Characterizing Seismic Scattering in 3D Heterogeneous Earth by a Single Parameter

Jagdish Chandra Vyas*[1], Martin Galis[2,3], and Paul Martin Mai[1]

ABSTRACT

We derive a theoretical parameter for three seismic scattering regimes where seismic wavelengths are either much shorter, similar, or much longer than the correlation length of small-scale Earth heterogeneities. We focus our analysis on the power spectral density (PSD) of the von Karman autocorrelation function (ACF), used to characterize the spatial heterogeneity of small-scale variations of elastic rock parameters that cause elastic seismic-wave scattering. Our analysis is based on the assumption that the PSD of the medium heterogeneities at the corresponding wavenumber is related to the wavefield scattering. Our theoretical findings are verified by numerical simulations. The seismic scattering effects in our simulations are assessed by examining attenuation of peak ground acceleration. We discover (1) that seismic scattering is proportional to the standard deviation of velocity variations in all three regimes, (2) that scattering is inversely proportional to the correlation length for the regime where seismic wavelengths are shorter than correlation length, but directly proportional to the correlation length in the other two regimes, and (3) that scattering effects are weak due to heterogeneities characterized by a gentle decay of the von Karman ACF for regimes where seismic wavelengths are similar or much longer than the correlation length.

KEY POINTS

- We derive a theoretical parameter that characterizes seismic scattering in 3D for three scattering regimes.
- Seismic scattering is a complex function of correlation length and Hurst exponent of random media.
- Our findings will help studies on ground-motion simulations in 3D to properly simulate elastic scattering.

Supplemental Material

INTRODUCTION

Heterogeneities in the Earth's crust and upper mantle cause seismic-wave scattering, manifested in so-called seismic coda waves that trail the main seismic phases. Often, coda waves are prominent features of seismic recordings; they decay slowly with time, whereby the statistics of the temporal decay provide information about the scattering process and the medium through which the waves traveled (e.g., Aki, 1969; Ritter *et al.*, 1997; Sato and Fehler, 1998; Sato *et al.*, 2012; Imperatori and Mai, 2013, 2015). After the Aki (1969) interpretation that coda waves are backscattered energy from uniformly distributed heterogeneities in the Earth, several theoretical models were presented to explain seismic scattering, such as the single scattering model, the multiple scattering model, the diffusion model, or the energy-flux model (Aki and Chouet, 1975; Sato, 1977; Gao *et al.*, 1983; Frankel and Wennerberg, 1987). In addition, the coda envelope broadens with increasing travel distance due to wavefield scattering (Sato, 2016), a process that can be modeled employing a Markov approximation as stochastic treatment of the wave equation in random media (Sato *et al.*, 2012; Sato, 2016). In contrast, *S*-wave coda excitation is mainly dominated by scattering of direct *S* waves from random heterogeneities in the Earth that can be modeled applying the Born approximation (Sato *et al.*, 2012; Sato and Emoto, 2017). In summary, coda waves are seismic-wave energy trapped in the Earth due to the small-scale heterogeneities in the Earth.

Small-scale heterogeneities in the Earth can be described by a random spatial field superimposed onto a background homogeneous medium. For this purpose, several random-field models have been proposed; these are conveniently characterized by an autocorrelation function (ACF). For example, von Karman, Gaussian, exponential and Henyey–Greenstein ACF or a fractal distribution are used to describe random fields of seismic-wave velocity variations in the Earth (e.g., Frankel and Clayton, 1986; Holliger and Levander, 1992; Sato and Fehler,

1. King Abdullah University of Science and Technology, Thuwal, Saudi Arabia; 2. Faculty of Mathematics, Physics and Informatics, Comenius University, Bratislava, Slovakia; 3. Earth Science Institute, Slovak Academy of Sciences, Bratislava, Slovakia

*Corresponding author: Jagdish.Vyas@kaust.edu.sa

Cite this article as Vyas, J. C., M. Galis, and P. M. Mai (2021). Characterizing Seismic Scattering in 3D Heterogeneous Earth by a Single Parameter, *Bull. Seismol. Soc. Am.* **111**, 791–800, doi: 10.1785/0120200153

1998; Sato, 2019). Most commonly, the von Karman ACF is used (e.g., Hartzell *et al.*, 2010; Imperatori and Mai, 2013; Bydlon and Dunham, 2015). The power spectral density (PSD) of the von Karman AFC in 3D is given by

$$p(k_m) = \frac{\sigma^2 (2\sqrt{\pi}a)^3 \Gamma(H+1.5)}{\Gamma(H)(1+k_m^2 a^2)^{(H+1.5)}}, \quad (1)$$

in which a, H, σ, and Γ are correlation length, Hurst exponent, standard deviation, and the Gamma function, respectively. We denote the wavenumber (2π/wavelength) of medium heterogeneity by k_m, and of the seismic wavefield by k_w, and write wavenumber k in case k_m and k_w can be used interchangeably.

Several studies examined the range for correlation lengths, standard deviation, and Hurst exponent in the Earth, both in observational studies and numerical simulations. Frankel and Clayton (1986) reported that velocity fluctuations with standard deviation of 5% and correlation lengths of 10 km (or greater) for 2D random media explain coda waves from microearthquakes and travel-time anomalies across seismic arrays. Holliger (1996) obtained correlation lengths of 10–100 m and Hurst exponent in the 0.1–0.2 range by analyzing sonic logs. Ritter *et al.* (1998) estimated wave-velocity perturbations of 3%–7% and correlation length of 1–16 km for the lithosphere in central France. Recently, Sato (2019) reported that velocity perturbations are 1%–10% in the Earth's crust and upper mantle and that the Hurst exponent typically falls in the 0.0–0.5 range, whereas correlation lengths vary widely depending on sample size or dimension of the measurement system. Overall, standard deviation, Hurst exponent, and correlation lengths are found to be in the 1%–10%, 0.0–0.5, and 1–15 km ranges, respectively.

Seismic-wave scattering occurs as the elastic waves encounter spatial variations of elastic medium properties. Although the deterministic reflection of a seismic wave at an internal interface of a seismic-velocity contrast could be classified as "seismic scattering," the common nomenclature is that seismic scattering is due to elastic-wave interactions with a spatially heterogeneous medium. In this context, the (statistical) characteristics of the scattered wavefield depend on the stochastic properties of the medium. This concept is conveniently described considering the wavelengths (λ) or wavenumbers (k_w) of the elastic wave, and characteristic scales (wavelengths) of the random media.

Based on wavelength λ or wavenumber k_w of the seismic wave, and the correlation length a of the random media, seismic-wave scattering can be classified into three regimes: (1) $k_w \times a \gg 1 (\lambda \ll a)$; (2) $k_w \times a \approx 1 (\lambda \approx a)$; (3) $k_w \times a \ll 1$ $(\lambda \gg a)$ (Sato and Fehler, 1998; Sato *et al.*, 2012). The regime $k_w \times a \gg 1$ characterizes high-frequency scattering in which seismic wavelengths are much shorter than correlation lengths. This regime is important for the earthquake engineering community in the context of high-frequency (10–20 Hz) ground-shaking estimation, because seismic scattering redistributes seismic-wave energy (i.e., ground-motion amplitudes) in space and time. The regime $k_w \times a \approx 1$ represents the diffraction condition, the most fundamental type of scattering. Finally, the regime $k_w \times a \ll 1$ denotes low-frequency scattering for which seismic wavelengths are much longer than the correlation length of the random medium. This regime is important for global seismology, which uses primarily long wavelengths (0.01–0.5 Hz) to invert for the deterministic velocity structure of the Earth or earthquake source parameters (e.g., centroid moment tensors).

Numerical and theoretical studies investigating the effects of seismic scattering on earthquake ground shaking suggest strong attenuation of ground motion due to wavefield scattering (Shapiro and Kneib, 1993; Mai, 2009; Hartzell *et al.*, 2010; Imperatori and Mai, 2012, 2013; Yoshimoto *et al.*, 2015; Vyas *et al.*, 2018). Bydlon and Dunham (2015) explained theoretically how the parameters describing the von Karman ACF control wavefield scattering in 2D. Using numerical simulations, they verified that a parameter $p_0 = \sigma/a^H$ determines the nature of scattering in the $k_w \times a \gg 1$ limit, regardless of the specific values of σ and a. However, how the other parameters of the von Karman ACF (a, σ, and H) affect 3D seismic scattering has not been explored yet in detail.

Here, we investigate seismic-wave scattering in 3D and verify our theoretical results by numerical simulations. First, we examine the mathematical expression for the PSD of the von Karman AFC (equation 1) to identify parameters that represent scattering behavior in 3D for the three different regimes, $k_w \times a \gg 1$, $k_w \times a \approx 1$, and $k_w \times a \ll 1$. Then, we test our theoretical findings through numerical simulations that cover the parameter space of these three regimes and allow us to examine how scattering manifests itself in seismic waveforms and ground-motion amplitudes.

THEORY

Bydlon and Dunham (2015) investigated high-frequency scattering ($f = 1$–30 Hz) by considering a 2D problem and the regime $k_w \times a \gg 1$. To analyze scattering under these assumptions, they simplified the PSD of the von Karman ACF to obtain the root mean square (rms) fluctuations of normalized seismic-wave velocity (wave speed), and then derived which parameters (i.e., a, H, and/or σ) control wavefield scattering. Here, we extend their approach to 3D by considering three different $k_w \times a$ regimes.

Wavefield scattering is the strongest if the wavenumber of the seismic wave is comparable to the wavenumber of heterogeneities in the medium. Hence, we simplify the PSD for the three regimes ($k_w \times a \gg 1$, $k_w \times a \approx 1$, and $k_w \times a \ll 1$) under the diffraction condition to obtain the rms of fluctuations of normalized wave velocity (computed as the square root of the mean power, denoted as P_{RM}). By assuming the diffraction condition, we derive theoretically the parameter P_{RM}, which in fact dictates the wavefield scattering in 3D. Seismic scattering associated with a particular seismic wavelength will depend on the amplitudes of velocity variations corresponding to that wavelength. However, we aim to understand the overall wavefield scattering behavior for a range of seismic wavelengths and heterogeneity scales in the medium. Therefore, our P_{RM} derivations are not only applicable for a monochromatic source or a single-wavelength medium, but instead capture the broadband nature of scattering. We only summarize the final equations for P_{RM} for each regime in the main article; further details of the derivations are provided in the supplemental material to this article.

Regime I: $k_w \times a \gg 1$

Our P_{RM} derivation for this regime assumes that the source excites waves of equal amplitude (a flat source spectrum) with wavenumbers from $k_{\min}$ to infinity, all of which interact with heterogeneities in the medium with the same range of wavenumbers (albeit at different "intensity" or strength). This assumption is not completely satisfied in nature as earthquakes typically excite only a limited range of frequencies, and not all of these frequencies will interact with the generally scale-limited medium heterogeneities. However, the assumption allows us to calculate the overall wavefield scattering behavior for the regime $k_w \times a \gg 1$, for which seismic wavelengths are much shorter than the correlation length of small-scale Earth heterogeneities. Then, the rms fluctuations of normalized wave velocity (P_{RM}) can be approximated by

$$P_{\mathrm{RM}} = \sqrt{\frac{1}{4\pi}\int_{k_{\min}}^{\infty} p(k) 4\pi k^2 dk} \approx \sqrt{4\pi}\sqrt{(c_0 + c_1 H + c_2 H^2)}\frac{\sigma}{a^H}\frac{\pi^{1/4}}{k_{\min}^H}. \tag{2}$$

Therefore, the P_{RM} dependency is given by

$$P_{\mathrm{RM}} \propto \sqrt{(c_0 + c_1 H + c_2 H^2)}\frac{\sigma}{a^H}, \tag{3}$$

in which we approximate the term depending on H by a quadratic function (with coefficients $c_0 = 0.89$, $c_1 = 0.53$, and $c_2 = -0.08$; see Fig. S1a and derivation in the supplemental material for details). We characterize the scattering behavior for the entire regime $k_w \times a \gg 1$, rather than for a particular wavelength in this regime using integration limits in equation (2) from $k_{\min}$ to infinity, and not over any arbitrary wavenumber range. Therefore, the parameter P_{RM} (equation 3) becomes independent of wavenumber. Comparing equation (3) with parameter $p_0 = \sigma/a^H$ (Bydlon and Dunham, 2015) reveals that even in the regime $k_w \times a \gg 1$, scattering in 3D is more complex than in 2D. Equation (3) illustrates that in the high-frequency scattering regime (a) scattering is proportional to the standard deviation of the velocity fluctuations, (b) scattering is inversely proportional to the correlation length a, and (c) the Hurst exponent has a strongly nonlinear effect on scattering. Interestingly, if the Hurst exponent approaches its theoretical lower limit of zero ($H \to 0$), equation (3) can be further simplified to

$$P_{\mathrm{RM}} \propto \sigma, \tag{4}$$

indicating that scattering is controlled by the standard deviation of the velocity variations in this case.

Regime II: $k_w \times a \approx 1$

We assume that the source excites waves having a flat source spectrum with wavenumbers from k_1 to k_2, all of which interact with medium heterogeneities of the same wavenumber range. If seismic wavelengths are comparable to the correlation length of heterogeneities, the rms fluctuations of normalized wave velocity can be approximated by

$$P_{\mathrm{RM}} = \sqrt{\frac{1}{4\pi}\int_{k_1}^{k_2} p(k) 4\pi k^2 dk}$$
$$\approx \sqrt{4\pi}\left(\frac{\pi}{18}\right)^{\frac{1}{4}} a^{\frac{3}{2}}\sigma\sqrt{(c_1 H + c_2 H^2)}\sqrt{(k_2^3 - k_1^3)}. \tag{5}$$

Therefore, the P_{RM} dependency is given by

$$P_{\mathrm{RM}} \propto \sqrt{(c_1 H + c_2 H^2)}a^{3/2}\sigma, \tag{6}$$

in which coefficients are given as $c_1 = 0.93$, and $c_2 = -0.27$ (see Fig. S1b). Analyzing equation (6) for P_{RM} reveals that (a) scattering is proportional to σ, similar to the regime $k_w \times a \gg 1$, (b) scattering is proportional to correlation length a, in contrast to regime $k_w \times a \gg 1$ (compare equation 6 with equation 3), and (c) scattering is correlated with the Hurst exponent (as H approaches zero, scattering effects weaken and become eventually negligible).

Regime III: $k_w \times a \ll 1$

Here, we assume that the source excites waves of equal amplitude (a flat source spectrum) with wavenumbers from zero to k_1, all of which interact with medium heterogeneities. If seismic wavelengths are much longer than the correlation length of the heterogeneities, the rms fluctuations of normalized wave velocity can be approximated by

$$P_{\mathrm{RM}} = \sqrt{\frac{1}{4\pi}\int_{0}^{k_1} p(k) 4\pi k^2 dk} \approx \sqrt{4\pi}\left(\frac{4\pi}{9}\right)^{\frac{1}{4}} a^{\frac{3}{2}}\sigma\sqrt{(c_1 H + c_2 H^2)}k_1^{\frac{3}{2}}. \tag{7}$$

Therefore, the P_{RM} dependency is given by

$$P_{\mathrm{RM}} \propto \sqrt{(c_1 H + c_2 H^2)}a^{3/2}\sigma, \tag{8}$$

in which coefficients $c_1 = 0.93$, and $c_2 = 0.40$ (see Fig. S1c). Only constant c_2 is different between equation (8) and equation (6), therefore, P_{RM} for the regime $k_w \times a \ll 1$ is similar to that for $k_w \times a \approx 1$, except that the effect of H on scattering is stronger for $k_w \times a \ll 1$ than for $k_w \times a \approx 1$ because $c_2 > 0$ (compare equation 6 and equation 8).

VERIFICATION OF THEORY BY SIMULATIONS

In this section, we verify our findings (equations 3, 4, 6, and 8) by conducting seismic-wavefield simulations in random media. Because our simulations do not strictly satisfy the assumptions used for the derivations of P_{RM}, we validate only proportionality or inverse proportionality of P_{RM} with correlation length, standard deviation, and Hurst exponent, rather than the complete expressions (equations 3, 4, 6, and 8). To numerically test our results for the three scattering regimes, we fix the correlation length a and modify the source frequency to radiate seismic waves with different frequencies (i.e., we are altering the wavenumber k_w). For computing synthetic seismograms, we use a generalized 3D finite-difference method with the second-order accuracy in space and time (Ely *et al.*, 2008). Our simulations consider several discretized Earth models, a point-source earthquake model, and receiver locations at which ground motions are stored. We then analyze waveforms and peak ground acceleration (PGA), and confront the numerical results with our theoretical analysis.

Setup for numerical modeling

We consider a point source (moment magnitude $M_w \sim 2.84$) at a depth of 7.5 km, with strike, dip, and rake of 22.5°, 90°, and 0°, respectively. The source time function (STF) is a Gaussian. We define STFs to radiate frequencies required to properly sample the three regimes ($f_{max} = 5.0$ Hz for $k_w \times a \gg 1$, $f_{max} = 0.5$ Hz for $k_w \times a \approx 1$, and $f_{max} = 0.03$ Hz for $k_w \times a \ll 1$, see Fig S2; f_{max} is the high-frequency limit of the flat portion of the slip velocity spectrum). For example, a point source radiating frequencies of 5.0, 0.5, and 0.03 Hz in a heterogeneous medium with background shear-wave velocity 3.464 km/s and stochastic perturbations with correlation length of 1 km yields $k_w \times a \approx 9.0$, 0.9, and 0.05, respectively.

To create a velocity model with small-scale heterogeneities, we add random-field variations of seismic-wave velocities, characterized by an isotropic von Karman ACF, to the uniform background Earth model (with S-wave velocity 3464 m/s, P-wave velocity, 6000 m/s, and density 2700 kg/m^3). In total, we generate 12 3D computational models (M1–M12; Table 1), considering three correlation lengths (1.0, 5.0, and 10.0 km), two values of standard deviation (5%, 10%), and two Hurst exponents (0.1, 0.5). For each combination of medium parameters, we create one realization of random inhomogeneity in S wave speed, P wave speed, and density. S-wave velocity distributions at the surface are shown for all 12 computational models (Fig. 1a,b). Theoretical 1D power spectra for seven selected models are plotted to illustrate effects of correlation lengths, standard deviation, and Hurst exponent on the spectral shape (Fig. 1c). Power spectra for two specific models, M2 and M11, are examined for the three scattering regimes considering the three STFs used in this study (Fig. 1d).

TABLE 1
Parameters for the 28 Computational 3D Earth Models Generated for This Study

Model Reference	Correlation Length a (km)	Standard Deviation σ (%)	Hurst Exponent H
M1, M1-L	1.0	5	0.1
M2, M2-L, M2-EL	5.0	5	0.1
M3, M3-EL	10.0	5	0.1
M4, M4-L	1.0	10	0.1
M5, M5-L, M5-EL	5.0	10	0.1
M6, M6-EL	10.0	10	0.1
M7, M7-L	1.0	5	0.5
M8, M8-L, M8-EL	5.0	5	0.5
M9, M9-EL	10.0	5	0.5
M10, M10-L	1.0	10	0.5
M11, M11-L, M11-EL	5.0	10	0.5
M12, M12-EL	10.0	10	0.5

Parameters of 28 computational 3D models generated using random fields characterized by von Karman autocorrelation functions (parameterized by correlation length, standard deviation, and Hurst exponent). The suffixes "-L" and "-EL" indicate large and extra-large models, respectively.

The size of the computational domain must be chosen such that seismic waves propagate to large-enough distances that ensure sufficient wave interaction with medium heterogeneities to develop scattering. At the same time, the domain should be as small as possible to minimize computational cost. Given these constraints, we define different computational domain sizes and grid spacings, depending on scattering regime. For the regime $k_w \times a \gg 1$, we use grid spacing $h = 25$ m ($dt = 0.0015$ s) on a domain of $60 \times 60 \times 15$ km, allowing travel distance of ~40 wavelengths (at $f = 5.0$ Hz). Combining these models with STF1 (Fig. S2a) yields $k_w \times a$ values in the range 9–90. For $k_w \times a \approx 1$, we use $h = 75$ m ($dt = 0.0045$ s) and a larger domain, $355 \times 355 \times 30$ km, corresponding to travel distance of ~50 wavelengths (at $f = 0.5$ Hz). The eight corresponding models are denoted by the suffix "-L" (see Table 1 and Fig. S3) and when combined with STF2 (Fig. S2b), they result in $k_w \times a$ values between 0.9 and 4.5. For $k_w \times a \ll 1$, we use $h = 1000$ m ($dt = 0.055$ s) and an extra-large domain, $2000 \times 2000 \times 60$ km (ignoring the spherical nature of the Earth), denoted by the suffix "-EL" (see Table 1 and Fig. S4). When combined with STF3 (Fig. S2c), the corresponding $k_w \times a$ values fall in the 0.27–0.5 range. Owing to the very long wavelengths in this regime (~115 km at $f = 0.03$ Hz), the domain allows travel distances of only ~15 wavelengths, significantly lower than those in the

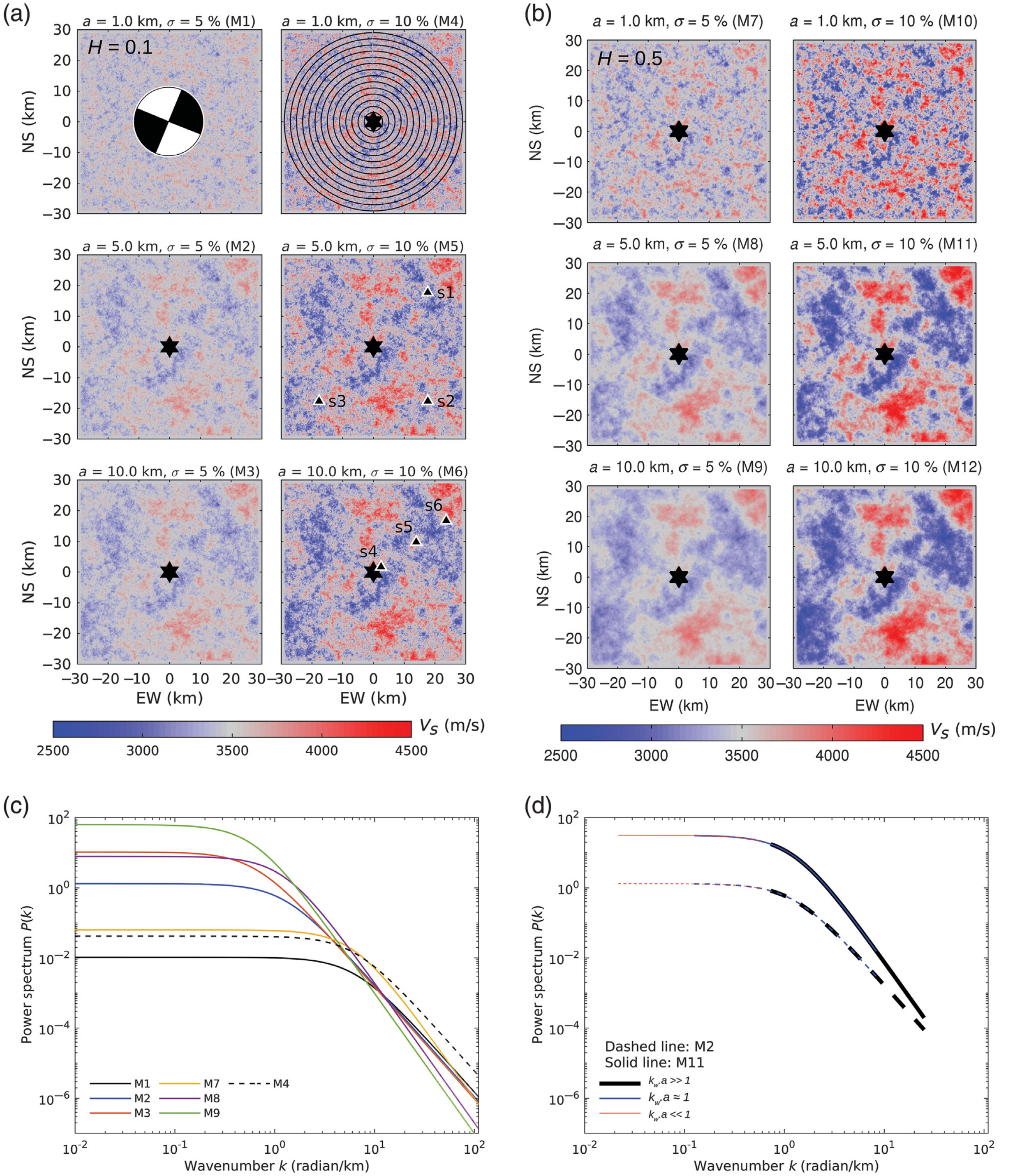

Figure 1. (a,b) *S*-wave speed distribution at the free surface for 12 3D computational models for the regime $k_w \times a \gg 1$, generated using three correlation lengths (1.0, 5.0, and 10.0 km), two standard deviations (5% and 10%) and two Hurst exponents (0.1 and 0.5). The black star marks the epicenter. The sites used for waveform comparison (black triangles, s1, s2, s3, s4, s5, and s6) and ground-motion analysis (black dots in circular rings) are also shown. The focal mechanism plot shows the earthquake source. Panels (a) and (b) depict random media with Hurst exponent 0.1 and 0.5, respectively. (c) Theoretical 1D power spectral density (PSD) for 3D Earth structure for seven selected models. Correlation length and Hurst exponent alter the shape of the power spectra (solid lines), whereas standard deviation only scales the PSD (mark dashed line; notice the scaling of M4 compared to M1, but their identical shape). (d) The theoretical power spectra of the random media are constrained by the dimensions of the computational model and the spatial grid size. Dashed and solid lines are spectra related to models M2 and M11, whereas three different colors depict power spectra sampled according to the three scattering regimes. EW, east–west; NS, north–south.

two previous regimes. However, the cost for computational models allowing travel distances of ~45–50 wavelengths would be exorbitant. In total, we use 28 computational models with random inhomogeneities, 12 of which are for $k_w \times a \gg 1$, eight for $k_w \times a \approx 1$, and eight for $k_w \times a \ll 1$ regimes. Our simulations consumed nearly four million core-hours of computational resources on a Cray XC40 supercomputer. To establish a base case for comparison, we also conduct simulations in a homogeneous medium for each regime.

We store synthetic seismograms at receivers placed in concentric rings for $k_w \times a \gg 1$, but for $k_w \times a \approx 1$ and $k_w \times a \ll 1$ we consider only a one quadrant to save computational costs (Fig. 1a, and Figs. S3a and S4a). The epicenter is placed in the center of the simulation domain for $k_w \times a \gg 1$, but for $k_w \times a \approx 1$ and $k_w \times a \ll 1$ it is in the lower left corner. Receiver geometry and epicenter location are designed to obtain the best possible azimuthal coverage of stations and to allow for sufficiently large travel distances for seismic waves to develop scattering, at the same time also minimizing computational costs. Virtual stations are distributed along rings with radial spacing of 0.1, 0.2, and 3.5 km, for $k_w \times a \gg 1$, $k_w \times a \approx 1$, and $k_w \times a \ll 1$ regimes, respectively. Therefore, each ring (arc) of stations contains a different number of stations at different azimuths. The smallest ring (arc) used for PGA statistics has 314 (radius 5 km), 196 (radius 25 km), and 134 (radius 300 km) stations for the three regimes ($k_w \times a \gg 1$; $k_w \times a \approx 1$; $k_w \times a \ll 1$). Therefore, our receiver geometry is statistically independent and PGA statistics are robust. All waveforms are low-pass filtered using a fourth-order Butterworth filter with cutoff frequencies of 5, 0.5, and 0.03 Hz for the three scattering regimes, respectively.

Quantifying seismic scattering in numerical results

Seismic scattering redistributes energy in space and time from direct P and S waves into the late-arriving coda waves. Consequently, PGA in a homogeneous medium will be, on average, higher than in a scattering medium. Therefore, we examine ratios of PGA values to quantify scattering "strength" in numerical simulations. Horizontal components of acceleration are mostly used in earthquake engineering applications (e.g., Boore and Atkinson, 2008; Chiou and Youngs, 2008), because wave amplitudes on the vertical component are usually smaller than on the horizontal components. Therefore, we analyze horizontal PGA (computed as maximum magnitude of acceleration from the two horizontal components). We illustrate scattering effects and resulting PGA values by comparing waveforms for selected receivers s1, s2, and s3 (see Fig. 1a for their locations).

In Figure 2, we compare horizontal-component ground-acceleration waveforms at selected stations for the regime $k_w \times a \gg 1$. Figure 2a compares waveforms and PGA values for two values of standard deviation (models M3 and M6) with those for the homogeneous medium. PGA values are consistent with our expectation that stronger scattering leads to lower

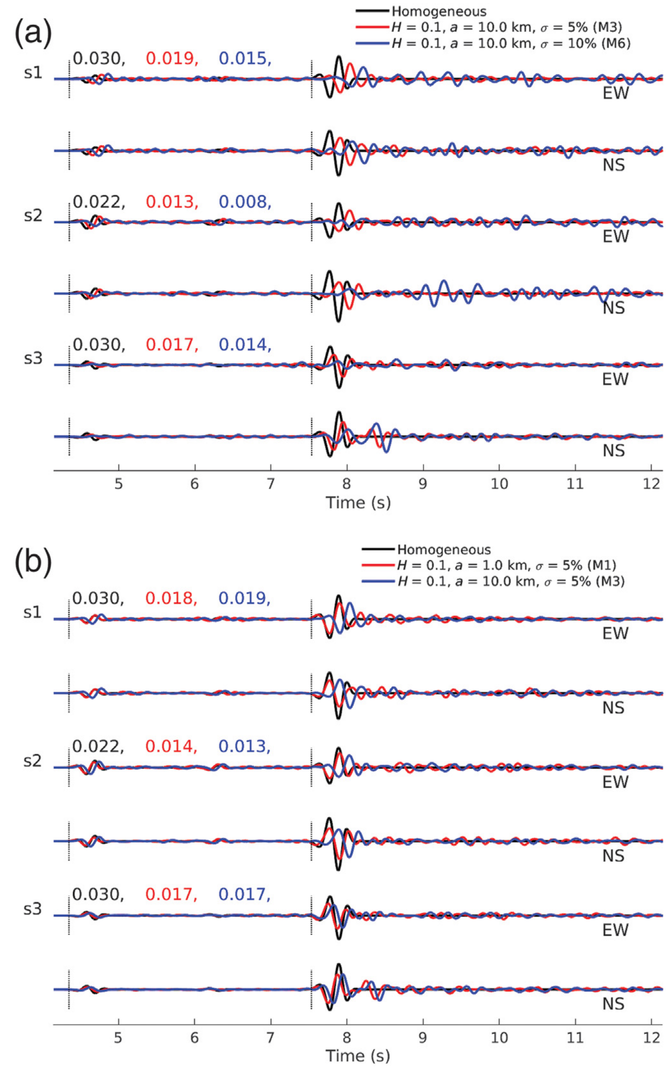

Figure 2. Horizontal components (EW and NS) of ground acceleration (m/s^2) at sites s1, s2, and s3 (Fig. 1a). Black dotted lines indicate theoretical P- and S-wave arrival times in the homogeneous medium. Color-coded numbers indicate peak ground acceleration (PGA) values at individual sites. Waveforms are normalized by their PGA value in the homogeneous-medium simulations for a given site. (a) Illustration of scattering controlled by σ for $k_w \times a \gg 1$ and small H; (b) Illustration of negligible effects of correlation length on scattering for $k_w \times a \gg 1$ and small H.

PGA. In this particular case, the scattering for model M3 is weaker than for model M6 (see also acceleration snapshots in Fig. S5). In addition, ground-acceleration comparison for M6 at three stations (Fig. S6) shows prominent coda evolution and reduced maximum acceleration values as epicentral distance increases (from s4 to s6). Figure 2b reveals that waveforms for two models with different correlation lengths (M1 and M3) are almost identical, with only small time shifts. This indicates that the two models yield almost identical levels of scattering (confirmed also by comparing acceleration snapshots for M1 and M3 in Fig. S5). Correspondingly, PGA values are comparable. In addition, these comparisons (Fig. 2a,b) suggest that scattering is primarily controlled by the standard deviation of the medium heterogeneities, whereas the correlation length has a negligible effect for a small H-value ($H = 0.1$), consistent with our theoretical analysis in equation (4). However, we note that PGA only works well in such comparisons because we computed a reference solution for the homogeneous medium. Without such a reference case, interpreting PGA values directly as indicator for "scattering strength" would be misleading.

Statistical analysis of scattering

Next, we calculate the mean and standard deviation of PGA values for all stations at a given epicentral distance and for a given computational model (see Fig. S7 for a comparative summary of all computational models). To estimate the average scattering-related PGA reduction at a given epicentral distance, we define the "mean PGA ratio" (MPR), at a particular epicentral distance, as the ratio between the mean PGA values from any heterogeneous Earth model to the mean PGA values from the reference homogeneous Earth model. As epicentral distance increases, the MPR is expected to decrease because the redistribution of seismic energy due to scattering is cumulative with propagation distance.

Figure 3 summarizes our results for $k_w \times a \gg 1$. For $H = 0.1$, we find the MPRs for models with $\sigma = 10\%$ (M4, M5, and M6) are lower than for models with $\sigma = 5\%$ (M1, M2, and M3) (Fig. 3a). At the same time, MPRs of both groups are very similar, supporting our theoretical conclusion that for small H the correlation length has insignificant effects on scattering, which in this regime is controlled by standard deviation (equation 4). The apparent plateau in MPRs for distances 10–20 km is a consequence of source effects being masked by wavefield scattering effects due to the hypocenter location (see Fig. S8 for more details on the effects of hypocentral depths on MPRs). Figure 3b compares solutions for $H = 0.5$, for which we expect a significant effect of both correlation length and standard deviation. For fixed σ, we observe that the MPRs for models with shorter correlation length are lower than those with longer correlation length ($MPR_{M7} < MPR_{M8} < MPR_{M9}$; similarly, $MPR_{M10} < MPR_{M11} < MPR_{M12}$). This finding is consistent with our conclusion that scattering is inversely proportional to correlation length for large H (equation 3). Also, MPRs for models with $\sigma = 10\%$ are lower than those for corresponding models with $\sigma = 5\%$ ($MPR_{M10} < MPR_{M7}$, $MPR_{M11} < MPR_{M8}$, $MPR_{M12} < MPR_{M9}$), demonstrating that scattering is proportional to the standard deviation of velocity variations for large H. Thus, these observations validate our theoretical conclusions for the regime $k_w \times a \gg 1$.

The MPR analysis for regime $k_w \times a \approx 1$ is summarized in Figure 4. For both values of H, the MPRs for models with shorter correlation length are higher than MPRs for models with longer correlation length ($MPR_{M1-L} > MPR_{M2-L}$, $MPR_{M4-L} > MPR_{M5-L}$, $MPR_{M7-L} > MPR_{M8-L}$, $MPR_{M10-L} > MPR_{M11-L}$), revealing that scattering is proportional to correlation length (see Fig. 4a,b). The MPRs for models with $\sigma = 5\%$ are higher than those for model with $\sigma = 10\%$ ($MPR_{M1-L} > MPR_{M4-L}$, $MPR_{M2-L} > MPR_{M5-L}$, $MPR_{M7-L} > MPR_{M10-L}$, $MPR_{M8-L} > MPR_{M11-L}$), indicating that scattering is proportional to the standard deviation of velocity fluctuations. The MPRs for models with $H = 0.1$ are larger than those for models with $H = 0.5$ ($MPR_{M1-L} > MPR_{M7-L}$, $MPR_{M2-L} > MPR_{M8-L}$, $MPR_{M4-L} > MPR_{M10-L}$, $MPR_{M5-L} > MPR_{M11-L}$), therefore, scattering is proportional to the Hurst exponent H. These observations are also consistent with our theoretical findings for $k_w \times a \approx 1$ (see equation 6).

Finally, we show MPR statistics for the regime $k_w \times a \ll 1$ (Fig. 5). First, recall that due to prohibitively large computational costs we used a smaller computational domain (see the Setup for Numerical Modeling section). Consequently, scattering is less well developed for $k_w \times a \ll 1$, and hence

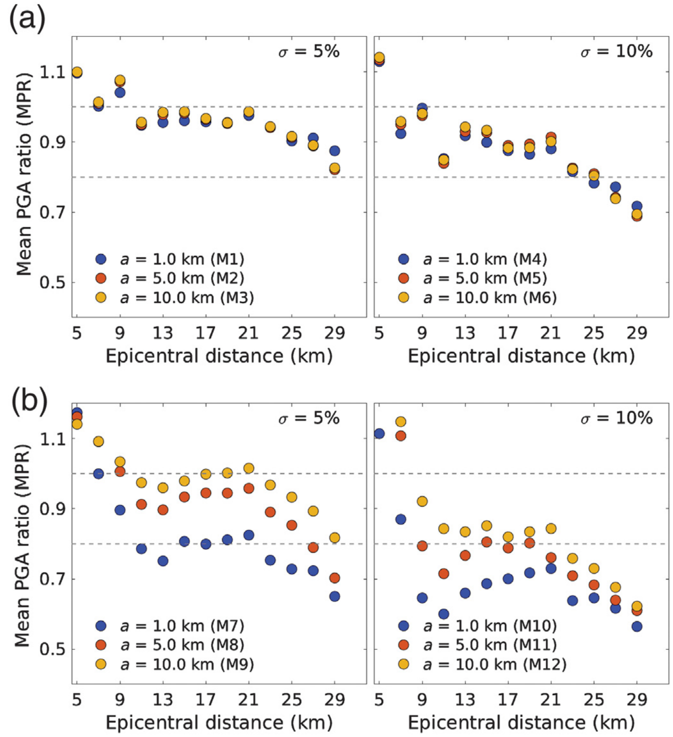

Figure 3. Mean PGA ratios (MPRs) for all 12 numerical simulations as a function of distance, depicting the effects of wavefield scattering on ground motions in the regime $k_w \times a \gg 1$. Panels (a) and (b) depict MPR for media with $H = 0.1$ and $H = 0.5$, respectively. Gray dashed lines are plotted to facilitate the MPR comparison in two nearby panels. Wavefield scattering is proportional to the standard deviation of medium heterogeneities, and inversely proportional to correlation length for large Hurst exponent ($H = 0.5$), but remains nearly unaffected by variations in correlation length for small Hurst exponent ($H = 0.1$). The $k_w \times a$ maxima for correlation lengths of 1, 5, and 10 km are 9.07, 45.36, and 90.72, respectively.

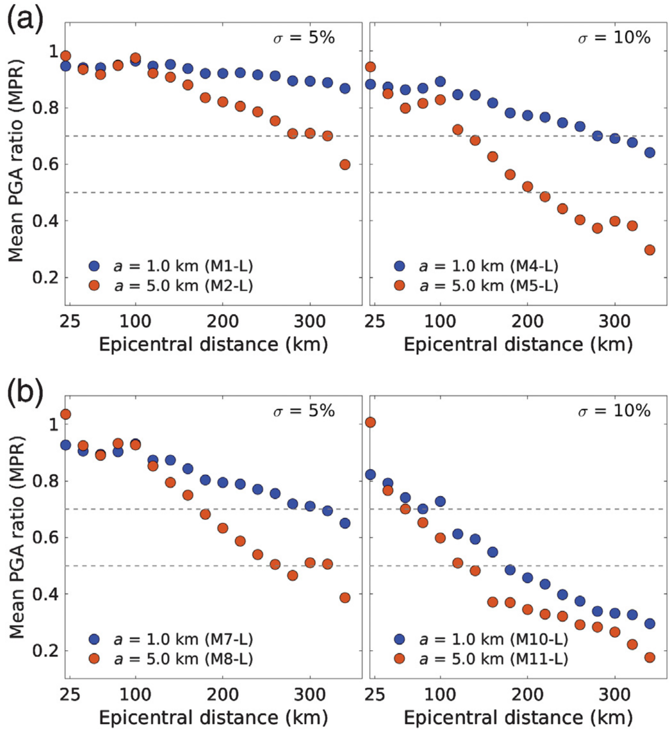

Figure 4. MPRs for eight numerical simulations as a function of distance, depicting the effects of wavefield scattering on ground motions in the regime $k_w \times a \approx 1$. Panels (a) and (b) depict MPR for media with $H = 0.1$ and $H = 0.5$, respectively. Gray dashed lines are plotted to facilitate the MPR comparison in two nearby panels. Wavefield scattering is proportional to correlation length, Hurst exponent, and standard deviation of medium heterogeneities. The highest values of $k_w \times a$ for correlation lengths of 1 and 5 km are 0.90 and 4.53, respectively.

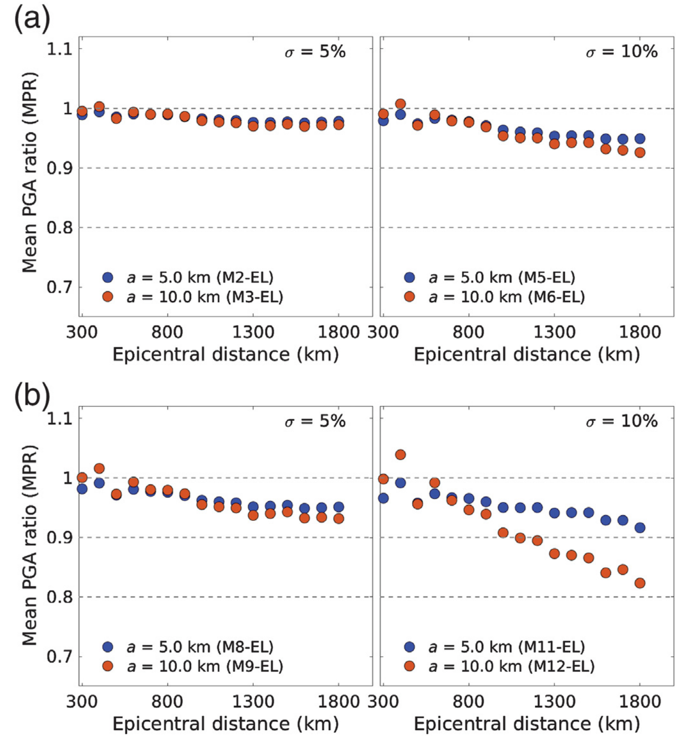

Figure 5. MPRs for all eight numerical simulations as a function of distance, depicting the effects of wavefield scattering on ground motions in the regime $k_w \times a \ll 1$. Panels (a) and (b) depict MPR for media with $H = 0.1$ and $H = 0.5$, respectively. Gray dashed lines are plotted to facilitate the MPR comparison in two nearby panels. Wavefield scattering is proportional to correlation length, Hurst exponent, and the standard deviation of medium heterogeneities. The highest values of $k_w \times a$ for correlation lengths of 5 and 10 km are 0.27 and 0.54, respectively.

effects on MPRs are not as pronounced as in the other two regimes. Still, the effects are strong enough to support our theoretical derivation (see waveform comparison in Fig. S9 and station locations in Fig. S4). The MPRs for models with 10 km correlation length are lower than those for 5 km correlation length ($\mathrm{MPR}_{\mathrm{M3-EL}} < \mathrm{MPR}_{\mathrm{M2-EL}}$, $\mathrm{MPR}_{\mathrm{M6-EL}} < \mathrm{MPR}_{\mathrm{M5-EL}}$, $\mathrm{MPR}_{\mathrm{M9-EL}} < \mathrm{MPR}_{\mathrm{M8-EL}}$, $\mathrm{MPR}_{\mathrm{M12-EL}} < \mathrm{MPR}_{\mathrm{M11-EL}}$), showing that scattering is proportional to correlation length. The MPRs for models with $\sigma = 10\%$ are lower than those for $\sigma = 5\%$ ($\mathrm{MPR}_{\mathrm{M12-EL}} < \mathrm{MPR}_{\mathrm{M9-EL}}$, $\mathrm{MPR}_{\mathrm{M11-EL}} < \mathrm{MPR}_{\mathrm{M8-EL}}$), suggesting that scattering is also proportional to the standard deviation of velocity variations. These observations agree well with our theoretical considerations for $k_w \times a \ll 1$ (see equation 8).

In summary, our results from numerical simulations are consistent with our conclusions based on theoretical derivation for all three considered scattering regimes.

DISCUSSION AND CONCLUSIONS

We derive a new parameter P_{RM} to quantify 3D seismic-wavefield scattering. P_{RM} is based on the assumption that small-scale heterogeneities in seismic velocity are characterized by the von Karman ACF. P_{RM} helps understand the influence of the parameters of the von Karman ACF on seismic scattering for three considered regimes ($k_w \times a \gg 1$, $k_w \times a \approx 1$, and $k_w \times a \ll 1$). We test our theoretical consideration through statistical analysis of a suite of numerical simulations that capture seismic scattering in different scattering regimes.

We find that the strength of wavefield scattering in all three regimes is proportional to the standard deviation of heterogeneities. Seismic scattering is also proportional to the correlation length in the regimes $k_w \times a \approx 1$ and $k_w \times a \ll 1$, but for the regime $k_w \times a \gg 1$ the scattering is inversely proportional to correlation length. For regime $k_w \times a \gg 1$, we also find that if the Hurst exponent H approaches zero, scattering will be controlled solely by standard deviation. However, for $k_w \times a \approx 1$ and $k_w \times a \ll 1$, scattering is only weakly affected for small values of H, with scattering vanishing in the limit of $H \to 0$.

To further explain these findings, we integrate the PSD for the 3D problem (equation 1) with respect to wavenumber k_m:

$$\int_0^\infty p(k_m)dk_m = 4\pi^2 a^2 \sigma^2 H. \quad (9)$$

Equation (9) represents the area under the power spectrum for a 3D isotropic PSD along one wavenumber axis; it reveals that the area under the power spectrum depends on a, H, and σ, implying also that the area under the power spectrum will be zero if any of a or H or σ is zero. For example, M2 has larger area under the power spectrum than M1 due to larger correlation lengths of M2, although standard deviation and Hurst exponent are identical for M1 and M2 (see Fig. 1c). The area under the power spectrum can be linked to wavefield scattering as it represents the total scattering power of the heterogeneous medium in terms of the sum of amplitude squares of seismic velocities. Correspondingly, in the limit of any of the von Karman parameters approaching zero, wavefield scattering will become negligible.

Quantitative analysis of power spectra in Figure 1c helps interpret the implications of equation (9) for the three scattering regimes. Therefore, our theoretical findings, confirmed by numerical simulations, can be explained by the amplitude and shape of the PSD. The standard deviation scales the power spectra without changing the shape of the power spectra (hence, area under the power spectra), resulting in scattering proportional to σ for all three regimes ($k_w \times a \gg 1$, $k_w \times a \approx 1$, and $k_w \times a \ll 1$). The tails of the power spectra (decaying part) show inverse proportionality with correlation length a (e.g., compare tails of M7, M8, and M9 in Fig. 1c), thus resulting in scattering being inversely proportional to a for the regime $k_w \times a \gg 1$. However, the plateau and corners (corner wavenumber $= 2\pi/a$) of the power spectra scale with correlation length, leading to scattering being proportional to correlation length for $k_w \times a \ll 1$ and $k_w \times a \approx 1$, respectively (e.g., compare plateau and corners of M7, M8, and M9 in Fig. 1c). Furthermore, the plateau and corner of power spectra grow as H increases; therefore, scattering is proportional to H for $k_w \times a \ll 1$ and $k_w \times a \approx 1$. Figure 1c also shows that the tails of the power spectra tend to merge for small H (see M1, M2, and M3) and diverge as H increases (compare M7, M8, and M9), implying a more complex dependency on H for scattering in the regime $k_w \times a \gg 1$. Hence, our findings can be explained by the shape and amplitude of the PSD function of the von Karman ACF.

Comparing our results for $k_w \times a \gg 1$ for the 3D problem (equation 3) with the 2D results by Bydlon and Dunham (2015) ($p_0 = \sigma/a^H$) reveals that the effect of standard deviation and correlation length remains the same, but the effect of the Hurst exponent H is stronger in 3D. However, if the Hurst exponent approaches zero, scattering effects are dominated by standard deviation, both in 2D and 3D. This is an important finding, because values of H smaller than 0.5 have been reported by Sato (2019) for the Earth's crust and mantle.

Here, we propose to quantify the overall wavefield scattering directly via an integral of the PSD function of the random media. We note that Sato *et al.* (2012) analyzed a plane wave scattered by a localized inhomogeneity using the wave equation. They solved the wave equation utilizing Born approximation, that is, they assumed that the amplitude of velocity variations is negligibly small compared to background velocity, that the amplitude of the scattered wavefield is negligibly small compared with the amplitude of incident wavefield, and that the scattered wavefield has only a small phase change after passing through the heterogeneity. They found that the scattering coefficient depends on the PSD function of the random media as follows (equation 4.25 from Sato *et al.*, 2012):

$$g(\theta, \omega) = \frac{k_w^4}{\pi} P\left(2k_w \sin\frac{\theta}{2}\right). \tag{10}$$

In equation (10), θ is the angle between incident and scattered waves; ω and k_w are angular frequency and wavenumber of the incident wavefield, respectively. The scattering coefficient reveals that a wave with wavenumber k_w interacts with medium heterogeneities with wavenumber k_m, leading to

$$k_m = 2k_w \sin\frac{\theta}{2} = 2\sin\frac{\theta}{2} k_w = Ck_w. \tag{11}$$

The scaling factor C is a function of the scattering angle θ and ranges from 0 to 2, for forward ($\theta = 0$) and backward ($\theta = \pi$) scattering, respectively. The average value of C (over θ) indicates the overall interaction between k_m and k_w, averaged over all directions. The average value of C is 1.27, therefore $k_m \sim k_w$. This is consistent with our assumption for the derivation of P_{RM}, although we apply an ideal diffraction condition ($k_m = k_w$). Our P_{RM} results will not change even if we use a more relaxed diffraction condition (i.e., $k_m \sim k_w$). Hence, our theory complies with Sato *et al.* (2012), but taking a different perspective on evaluating the wavefield scattering. The detailed theoretical analysis to fully describe the wavefield scattering in 3D requires considering the 3D elastic-wave equation with complex earthquake source characteristics (radiated wavefield) in 3D random media with anisotropic wave propagation. This derivation is beyond the scope of the present study.

In summary, our theoretical analysis of the von Karman PSD, used to represent random spatial variation in seismic-wave velocities and rock density, helps develop a physics-based understanding of how standard deviation, correlation length, and Hurst exponent govern 3D seismic-wavefield scattering for three scattering regimes ($k_w \times a \gg 1$, $k_w \times a \approx 1$, and $k_w \times a \ll 1$). This will help studies on ground-motion simulations for earthquake shaking as well as research on global seismic wave propagation in 3D Earth models to properly simulate elastic-wavefield scattering.

DATA AND RESOURCES

Ground-motion simulations carried out to verify the outcomes of theoretical derivation generated nearly 2.5 TB of data that can be provided via personal communication. This article has a supplemental material that comprises the complete derivation of the root mean square fluctuations of normalized wave velocity using power spectral density of the von Karman autocorrelation function for three scattering regimes ($k_w \times a \gg 1$, $k_w \times a \approx 1$, and $k_w \times a \ll 1$). The supplemental material also contains figures of the quadratic fit to ratios of gamma functions, three Gaussian source time functions, simulations setup depicting receiver geometry and *S*-wave speed variations, acceleration waveforms comparison from few receivers, snapshots of ground-acceleration wavefield at the Earth surface, and peak ground acceleration statistics.

ACKNOWLEDGMENTS

The research presented in this article is supported by King Abdullah University of Science and Technology (KAUST) in Thuwal, Saudi Arabia, Grants BAS/1/1339-01-01 and URF/1/3389-01-01. M. G. was partially supported by Scientific Grant Agency VEGA, Grant 2/0046/20. Earthquake ground-motion simulations have been carried out using the KAUST Supercomputing Laboratory (KSL), and the authors acknowledge the support of the KSL staff. The authors thank Art Frankel and an anonymous reviewer, as well as Associate Editor Adrien Oth, for their constructive critical review that helped greatly to improve the article.

REFERENCES

Aki, K. (1969). Analysis of the seismic coda of local earthquakes as scattered waves, *J. Geophys. Res.* **74,** no. 2, 615–631.

Aki, K., and B. Chouet (1975). Origin of coda waves: Source, attenuation, and scattering effects, *J. Geophys. Res.* **80,** no. 23, 3322–3342.

Boore, D. M., and G. M. Atkinson (2008). Ground-motion prediction equations for the average horizontal component of PGA, PGV, and 5%-damped PSA at spectral periods between 0.01 s and 10.0 s, *Earthq. Spectra* **24,** no. 1, 99–138.

Bydlon, S. A., and E. M. Dunham (2015). Rupture dynamics and ground motions from earthquakes in 2-D heterogeneous media, *Geophys. Res. Lett.* **42,** no. 6, 1701–1709.

Chiou, B. J., and R. R. Youngs (2008). An NGA model for the average horizontal component of peak ground motion and response spectra, *Earthq. Spectra* **24,** no. 1, 173–215.

Ely, G. P., S. M. Day, and J. B. Minster (2008). A support-operator method for viscoelastic wave modelling in 3-D heterogeneous media, *Geophys. J. Int.* **172,** no. 1, 331–344.

Frankel, A., and R. W. Clayton (1986). Finite difference simulations of seismic scattering: Implications for the propagation of short-period seismic waves in the crust and models of crustal heterogeneity, *J. Geophys. Res.* **91,** no. B6, 6465–6489.

Frankel, A., and L. Wennerberg (1987). Energy-flux model of seismic coda: Separation of scattering and intrinsic attenuation, *Bull. Seismol. Soc. Am.* **77,** no. 4, 1223–1251.

Gao, L. S., N. N. Biswas, L. C. Lee, and K. Aki (1983). Effects of multiple scattering on coda waves in three-dimensional medium, *Pure Appl. Geophys.* **121,** no. 1, 3–15.

Hartzell, S., S. Harmsen, and A. Frankel (2010). Effects of 3D random correlated velocity perturbations on predicted ground motions, *Bull. Seismol. Soc. Am.* **100,** no. 4, 1415–1426.

Holliger, K. (1996). Upper-crustal seismic velocity heterogeneity as derived from a variety of *P*-wave sonic logs, *Geophys. J. Int.* **125,** no. 3, 813–829.

Holliger, K., and A. R. Levander (1992). A stochastic view of lower crustal fabric based on evidence from the Ivrea zone, *Geophys. Res. Lett.* **19,** no. 11, 1153–1156.

Imperatori, W., and P. M. Mai (2012). Sensitivity of broad-band ground-motion simulations to earthquake source and Earth structure variations: an application to the Messina Straits (Italy), *Geophys. J. Int.* **188,** no. 3, 1103–1116.

Imperatori, W., and P. M. Mai (2013). Broad-band near-field ground motion simulations in 3-dimensional scattering media, *Geophys. J. Int.* **192,** no. 2, 725–744.

Imperatori, W., and P. M. Mai (2015). The role of topography and lateral velocity heterogeneities on near-source scattering and ground-motion variability, *Geophys. J. Int.* **202,** no. 3, 2163–2181.

Mai, P. M. (2009). Ground motion: Complexity and scaling in the near field of earthquake ruptures, in *Encyclopedia of Complexity and System Sciences*, R. Meyers (Editor), Springer, 4435–4474, ISBN: 978-0-387-69572-3.

Ritter, J. R., P. M. Mai, G. Stoll, and K. Fuchs (1997). Scattering of teleseismic waves in the lower crust observations in the Massif Central, France, *Phys. Earth Planet. In.* **104,** nos. 1/3, 127–146.

Ritter, J. R., S. A. Shapiro, and B. Schechinger (1998). Scattering parameters of the lithosphere below the Massif Central, France, from teleseismic wavefield records, *Geophys. J. Int.* **134,** no. 1, 187–198.

Sato, H. (1977). Single isotropic scattering model including wave conversions simple theoretical model of the short period body wave propagation, *J. Phys. Earth* **25,** no. 2, 163–176.

Sato, H. (2016). Envelope broadening and scattering attenuation of a scalar wavelet in random media having power-law spectra, *Geophys. J. Int.* **204,** no. 1, 386–398.

Sato, H. (2019). Power spectra of random heterogeneities in the solid earth, *Solid Earth* **10,** no. 1, 275–292.

Sato, H., and K. Emoto (2017). Synthesis of a scalar wavelet intensity propagating through von Kármán-type random media: Joint use of the radiative transfer equation with the Born approximation and the Markov approximation, *Geophys. J. Int.* **211,** no. 1, 512–527.

Sato, H., and M. C. Fehler (1998). *Seismic Wave Propagation and Scattering in the Heterogenous Earth*, Springer-Verlag, New York, New York, ISBN: #0-387-98329-5.

Sato, H., M. C. Fehler, and T. Maeda (2012). *Seismic Wave Propagation and Scattering in the Heterogeneous Earth*, Springer Science & Business Media, ISBN: 978-3-642-23028-8.

Shapiro, S. A., and G. Kneib (1993). Seismic attenuation by scattering: Theory and numerical results, *Geophys. J. Int.* **114,** no. 2, 373–391.

Vyas, J. C., P. M. Mai, M. Galis, E. M. Dunham, and W. Imperatori (2018). Mach wave properties in the presence of source and medium heterogeneity, *Geophys. J. Int.* **214,** no. 3, 2035–2052.

Yoshimoto, K., S. Takemura, and M. Kobayashi (2015). Application of scattering theory to *P*-wave amplitude fluctuations in the crust, *Earth Planets Space* **67,** no. 1, 199.

Manuscript received 18 April 2020
Published online 05 January 2021